



# Motion estimation based on projective information disentanglement for 3D reconstruction of rotational coronary angiography

Xiujian Liu<sup>a</sup>, Si Li<sup>a</sup>, Bin Wang<sup>b,c</sup>, Lin Xu<sup>d,\*</sup>, Zhifan Gao<sup>a,\*</sup>, Guang Yang<sup>e,f</sup>

<sup>a</sup> School of Biomedical Engineering, Sun Yat-sen University, Shenzhen, China

<sup>b</sup> Department of Cardiology, the First Affiliated Hospital of Shantou University Medical College, Shantou, China

<sup>c</sup> The Clinical Research Center of the First Affiliated Hospital of Shantou University Medical College, Shantou, China

<sup>d</sup> General Hospital of the Southern Theatre Command, PLA and The First School of Clinical Medicine, Southern Medical University, Guangzhou, China

<sup>e</sup> National Heart and Lung Institute, Imperial College London, London, UK

<sup>f</sup> Cardiovascular Research Centre, Royal Brompton Hospital, London, UK

## ARTICLE INFO

### Keywords:

Coronary angiography  
3D reconstruction  
Motion compensation  
Projection space  
Vessel overlapping

## ABSTRACT

The 2D projection space-based motion compensation reconstruction (2D-MCR) is a kind of representative method for 3D reconstruction of rotational coronary angiography owing to its high efficiency. However, due to the lack of accurate motion estimation of the overlapping projection pixels, existing 2D-MCR methods may still have a certain level of under-sampling artifacts or lose accuracy for cases with strong cardiac motion. To overcome this, in this study, we proposed a motion estimation approach based on projective information disentanglement (PID-ME) for 3D reconstruction of rotational coronary angiography. The reconstruction method adopts the framework of 2D-MCR, which is referred to as 2D-PID-MCR. The PID-ME consists of two parts: generation of the reference projection sequence based on the fast simplified distance driven projector (FSDDP) algorithm, motion estimation and correction based on the projective average minimal distance measure (PAMD) model. The FSDDP algorithm generates the reference projection sequence faster and accelerates the whole reconstruction greatly. The PAMD model can disentangle the projection information effectively and estimate the motion of both overlapping and non-overlapping projection pixels accurately. The main contribution of this study is the construction of 2D-PID-MCR to overcome the inherent limitations of the existing 2D-MCR method. Simulated and clinical experiments show that the PID-ME, consisting of FSDDP and PAMD, can estimate the motion of the projection sequence data accurately and efficiently. Our 2D-PID-MCR method outperforms the state-of-the-art approaches in terms of accuracy and real-time performance.

## 1. Introduction

The 3D reconstruction of rotational coronary angiography can provide the required volumetric information for clinical application. The current clinical application relies on the standard coronary angiography (CAG) to perform catheter-based cardiovascular therapy [1]. Due to the 2D projection imaging characteristics, the cumulative effect of suboptimal projection angles, vessel overlap and foreshortening, and vessel tortuosity may lead to overestimation or underestimation of stenosis severity [2,3]. In contrast, 3D reconstruction of rotational coronary angiography can overcome these limitations and provide an objective representation of the actual vascular structure [4–6]. However, the motion state inconsistency of the projection sequence data hinders the 3D reconstruction of rotational coronary angiography. 3D reconstruction relies on the motion state consistency assumption of the projection sequence data [7–9]. However, the projection sequence data acquired

by rotational coronary angiography include several inconsistent motion states due to cardiac motion. Thus, the correct correspondence between 2D pixels of the projection sequence and 3D reconstructed voxels of the reference phase is disrupted. The calculation error of the reconstruction caused by this incorrect correspondence will result in motion artifacts and damage the volumetric information provided by the 3D reconstruction of coronary angiography.

Existing reconstruction methods have shortcomings in solving the problem of motion state inconsistency. Currently, there are two main categories of angiographic reconstruction methods: gated reconstruction and motion compensation reconstruction. Gated reconstruction methods adopt a simple strategy of selecting a subset of images with the same motion state to build the correspondence. However, gated reconstruction methods usually achieve under-sampling streak artifacts due to discarding a large number of projection data [10–12]. Motion

\* Corresponding authors.

E-mail addresses: [lynne1111@126.com](mailto:lynne1111@126.com) (L. Xu), [gaozhifan@mail.sysu.edu.cn](mailto:gaozhifan@mail.sysu.edu.cn) (Z. Gao).

compensation reconstruction (MCR) methods build the correspondence by modeling the mapping relationship in 3D image space or 2D projection space. 3D image space-based MCR (3D-MCR) methods estimate the voxel motion mapping relationship from the reference motion state to others. However, the parameter estimation of 3D-MCR is a strongly ill-posed problem with high computational demands, so it is often difficult to obtain a very satisfactory result in practice [13,14]. The 2D projection space-based motion compensation reconstruction (2D-MCR) methods estimate the pixel motion mapping relationship of the projection data from the reference motion state to other states. 2D-MCR corrects the projection data to the reference state according to the estimation so that the correspondence between the corrected 2D projection and 3D reconstructed image is right.

However, due to the lack of accurate motion estimation of the overlapping projection pixels, existing 2D-MCR may still have a certain level of under-sampling artifacts or lose the accuracy for cases with strong cardiac motion [15,16]. First, the existing 2D-MCR methods use the ordinary registration strategy to estimate the pixel motion from the reference projection to the acquired projection and correct the projection data by transforming the pixels according to the motion estimation. The overlapping projection pixels are considered the same structure instead of different structures [15]. Therefore, the existing 2D-MCR methods are only an approximation. Second, the existing 2D-MCR methods usually adopt the gating window to resolve residual motion, the pixel motion from the current motion state to the reference state. The residual motion within the gating window could be assumed to be reasonably small and smooth [16]. However, too few projections of the gating window may also lead to under-sampling artifacts. Third, the residual motion might be large even inside the gating window when the cardiac motion is strong. The approximate 2D motion estimation is not sufficient. Lastly, the traditional pixel-to-pixel motion estimation model could not separate the overlapping pixels and find their correspondences [17,18]. Accurate motion estimation needs to match the overlapping pixels of one motion state to its corresponding non-overlapping pixels of another state, and find the optimal estimation model that conforms to the complex cardiac nonlinear deformation.

Therefore, this study proposes a motion estimation approach based on projective information disentanglement (PID), referred to as PID-ME, to disentangle the overlapping projection pixels and estimate the motion correspondence of the projection data at all the cardiac motion states. The PID-ME method consists of two parts: generation of the reference projection sequence based on the fast simplified distance-driven projector (FSDDP) algorithm, motion estimation and correction based on the projective average minimal distance (PAMD) model. First, as PID-ME estimates the motion correspondence at more cardiac motion states, generating the reference projection sequence needs high efficiency. The FSDDP algorithm is based on the efficient and accurate simplified distance-driven projector (SDDP). It exploits the features of the projective geometry to reduce the repetitive calculation when calculating the system matrix of the projector. Consequently, the FSDDP algorithm can generate the reference projection sequence in real-time without a decrease in accuracy. Second, as the traditional pixel-to-pixel mapping model cannot deal with overlapping pixels, the PAMD model disentangles the overlapping projective information by modeling the mapping relationship from the projection domain of one voxel at one state to the projection domain at another state. The transformed projection data is composited by the transformed projection domains of all the voxels. Then, the PAMD model estimates the transformation parameters by similarity measures with a family of average minimal distance measures, which are smooth and have less local minimum. These help the PAMD model converge to a superior solution quickly. As a result, PID-ME can estimate the residual motion of the projection data accurately and efficiently. The proposed 3D reconstruction method based on the PID-ME method, referred to as the 2D-PID-MCR method, overcomes the inherent limitations of existing 2D-MCR methods. Fig. 1 illustrates the challenge and contribution of our 2D-PID-MCR method for 3D reconstruction of rotational coronary angiography.

## 2. Related works

This section reviews the existing MCR methods for 3D reconstruction of rotational coronary angiography. The MCR methods require a representation of the motion field to model the mapping of the 3D voxels or 2D pixels from a reference motion state to other motion states [2]. The temporal component of the motion field is commonly parameterized by the cardiac phase assuming a periodic motion [19,20].

### 2.1. 3D image space-based MCR methods

The motion field of 3D-MCR is usually parameterized by a 4D motion vector field [21]. As B-spline transformations offer spatial smoothness, researchers use 3D [20] or 4D B-spline transformation [13] to represent the motion vector field. One strategy for parameter estimation is propagating a 3D reconstruction to the remaining projection images by a 3D-2D registration [19,20]. Another strategy is reconstructing a series of ECG-gated reconstructions at several phases. These reconstructions are then used to estimate the transformation parameters by a defined intensity-based registration [7]. Other strategies are estimating the parameters jointly with reconstruction [14,20]. The transformation parameters are embedded into the reconstruction formulations. The objective function is derived from the projection error between the forward projections of the reconstruction and the acquired projection images [14]. The parameters are updated by an optimization algorithm, and the reconstruction result is updated by the reconstruction formula iteratively. After estimation, the 4D motion vector fields will be incorporated into the reconstruction formulation to realize MCR. In theory, 3D-MCR can compensate for arbitrary motion so this kind of method has high accuracy. However, a fully 3D estimation is a strongly ill-posed problem with high computational demands.

### 2.2. 2D projection space-based MCR methods

The 2D-MCR usually parameterizes the motion field by a 2D geometric transformation. Movassaghi [22] and Hansis [15] employ 2D rigid and 2D elastic transformations respectively. Schwemmer uses 2D affine and 2D B-spline [16] to model the motion field. Usually, 2D-MCR methods obtain an initial 3D reconstruction at the reference phase [23,24]. Then, the initial 3D reconstruction is forward projected onto the projection images at different phases. The parameters of the motion field are estimated by the registration between the acquired projection image and the reference forward projected image. Due to the difficulty of the segmentation of the vasculature centerlines [25], the registration strategies have developed from feature-based [13] to intensity-based [16] [27-28]. The advanced intensity-based methods are often fully automatic, have no user interaction, and do not require complex pre-processing steps [26,27]. The estimated transformation is applied to the projection images and these corrected images are used for the final MCR. Generally, 2D-MCR methods compute the reconstruction and iteratively perform motion compensation to refine the final result [15]. 2D-MCR methods usually start with a small gating window for the initial reconstruction and gradually increase the width of the window as iterations progress for the motion compensation. However, too few projections of the gating window may lead to under-sampling artifacts. Additionally, when the cardiac motion is strong, the residual motion might be large even inside the gating window. This in turn makes the motion estimation insufficient and obtains an inaccurate 3D reconstruction.

## 3. Methods

The framework of our 2D-PID-MCR method is described in Fig. 2. First, input and preprocess the original angiography sequences. Second, we adopt the projection images gated by the estimated vessel motion signal to reconstruct an initial 3D model [7]. Third, using the PID-ME algorithm to estimate and correct the motion corresponding of the projection data. The PID-ME algorithm consists of two parts: generation

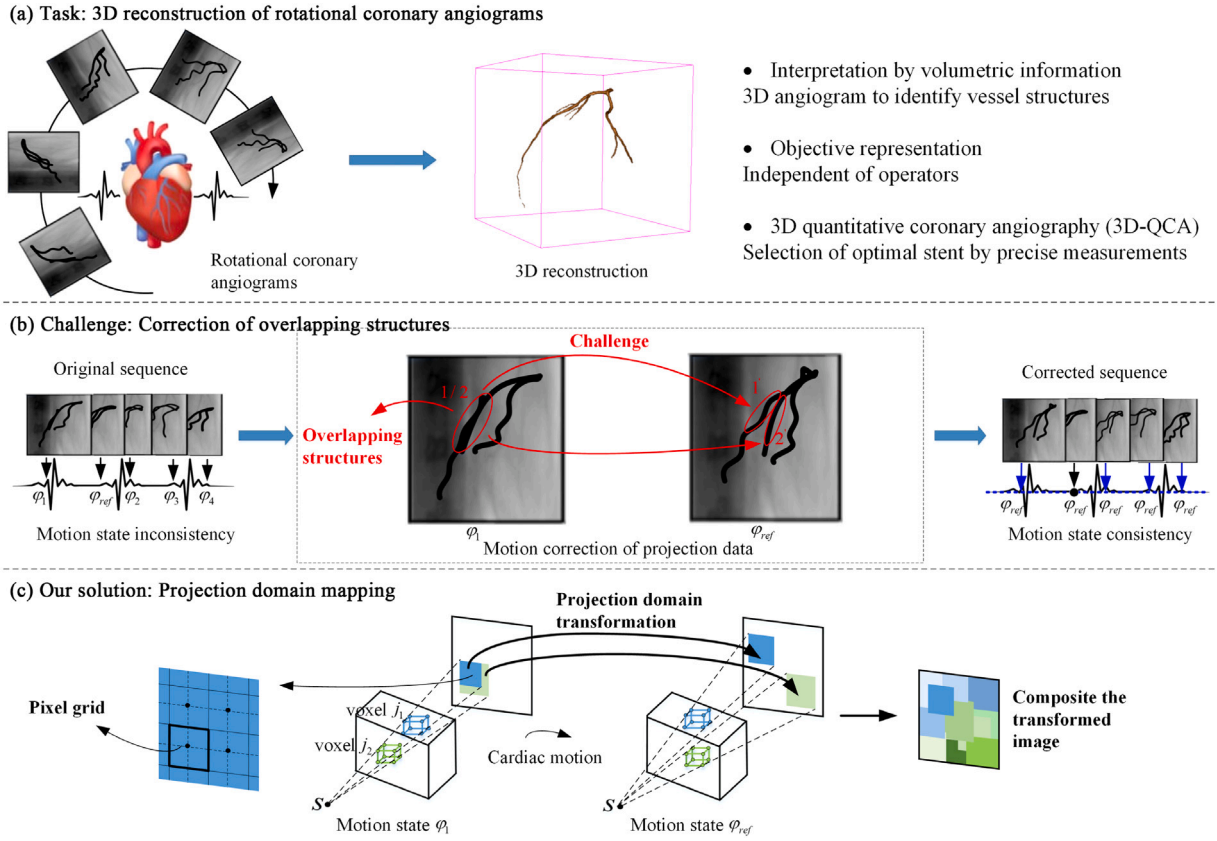


**Fig. 1.** The contribution of our 2D-PID-MCR method to correct overlapping structures. (a) The PID-ME aims to perform 3D reconstruction of the rotational coronary angiography. (b) The challenge of 3D reconstruction is to correct overlapping structures in the images. (c) We proposed the 2D-PID-MCR method to transform the projection domain map for 3D reconstruction.

of reference sequence by the FSDDP algorithm (Fig. 2b), and motion estimation and correction by the PAMD model (Fig. 2c). Finally, we perform the MCR by using the corrected projection sequence. The whole 2D-PID-MCR method performs an iterative process to obtain the final refined result.

### 3.1. Input and preprocessing

The input and preprocessing of the projection sequence include background removal and vessel motion signal estimation. We adopt the simple top-hat filter [28] to suppress the background of the coronary angiography.

In this study, we suppose that there is no respiratory motion during the image acquisition. Lehmann [29] has proven that image-based gating is more advantageous than ECG gating for 3D reconstruction of coronary angiography. We adopt this angle-independent surrogate motion signal (SMS) measure algorithm to represent the vessel motion.  $p_{bgr}^\theta$  ( $\theta = \theta_1, \dots, \theta_K$ ) represents the projection image at the acquisition angle  $\theta$  after background removal. For the rotational projection sequence, each projection image  $p_{bgr}^\theta$  is assigned a motion phase  $\varphi(\theta)$ . The motion phase  $\varphi(\theta) \in [0, 1]$  of  $p_{bgr}^\theta$  denotes the relative heart motion state.  $t$  is the acquisition time. We set  $t(\theta_1) = 0$ , then each projection image  $p_{bgr}^\theta$  has its corresponding acquisition time  $t(\theta)$  and motion phase  $\varphi(t(\theta))$ . The  $v$  axis of the detector is most closely aligned with the rotation axis of the imaging system. This image-based motion metric is the  $v$  component of the weighted centroid of  $p_{bgr}^\theta$  and calculated as:

$$SMS(t(\theta)) = \frac{\sum_{u=1}^{N_u} \sum_{v=1}^{N_v} v * p_{bgr}^\theta(u, v)}{\sum_{u=1}^{N_u} \sum_{v=1}^{N_v} p_{bgr}^\theta(u, v)} \quad (1)$$

where  $N_u$  and  $N_v$  are the image dimensions. Next,  $SMS$  should be further processed using a boxcar-normalization technique to ensure

the consistency of the waveform. Concretely, in order to calculate the boxcar-normalized signal  $SMS_N(t)$ , each value of  $SMS(t)$  is rescaled to be in the range of  $[0, 1]$  using the maximum and minimum of  $SMS(t - \Delta t) : SMS(t + \Delta t)$ .  $\Delta t$  is the width of the boxcar, which is set to the patient's mean cardiac cycle length.  $\Delta t$  can be estimated as the inverse of the fundamental frequency which can be calculated by Fourier transform [29].

The gating window  $\omega_1$  indicates the motion phases with minimal motion during the cardiac cycle. The position of the gating window can be calculated automatically according to the first and second derivatives of  $SMS_N(t)$  ( $dSMS_N(t)$  and  $d^2SMS_N(t)$  respectively). We set the largest local minima of  $d^2SMS_N(t)$  for each cardiac cycle as the trigger point ( $\rho$ ). We perform a backward search beginning at  $\rho$  to define the gating window  $\omega_1$ . The first point where  $|dSMS_N(t)|$  is less than the threshold  $v_t$  is the starting position of  $\omega_1$ , and the first point where  $|dSMS_N(t)|$  is bigger than  $v_t$  is the end position of  $\omega_1$ . The center position of  $\omega_1$  corresponds to the reference phase  $\varphi_{ref}(t)$ .  $\varphi_{ref}$  and  $\omega_1$  may vary across each cardiac cycle.

### 3.2. Initial 3D reconstruction

We adopt the streak-reduced gated FDK algorithm [7] to reconstruct the initial 3D image  $f_{\varphi_{ref}}^{(0)}$  at the reference cardiac motion phase. This algorithm has been proved to be effective in reducing the streak artifacts which result from the under-sampled data. We select the phase-consistent subset of the projection data to reconstruct this initial 3D image. The reference phase  $\varphi_{ref}$  and the gating window  $\omega_1$  of each cardiac cycle are determined by the above preprocessing procedure. The initial 3D reconstructed image  $f_{\varphi_{ref}}^{(0)}$  can be calculated by the formulas described in [7].



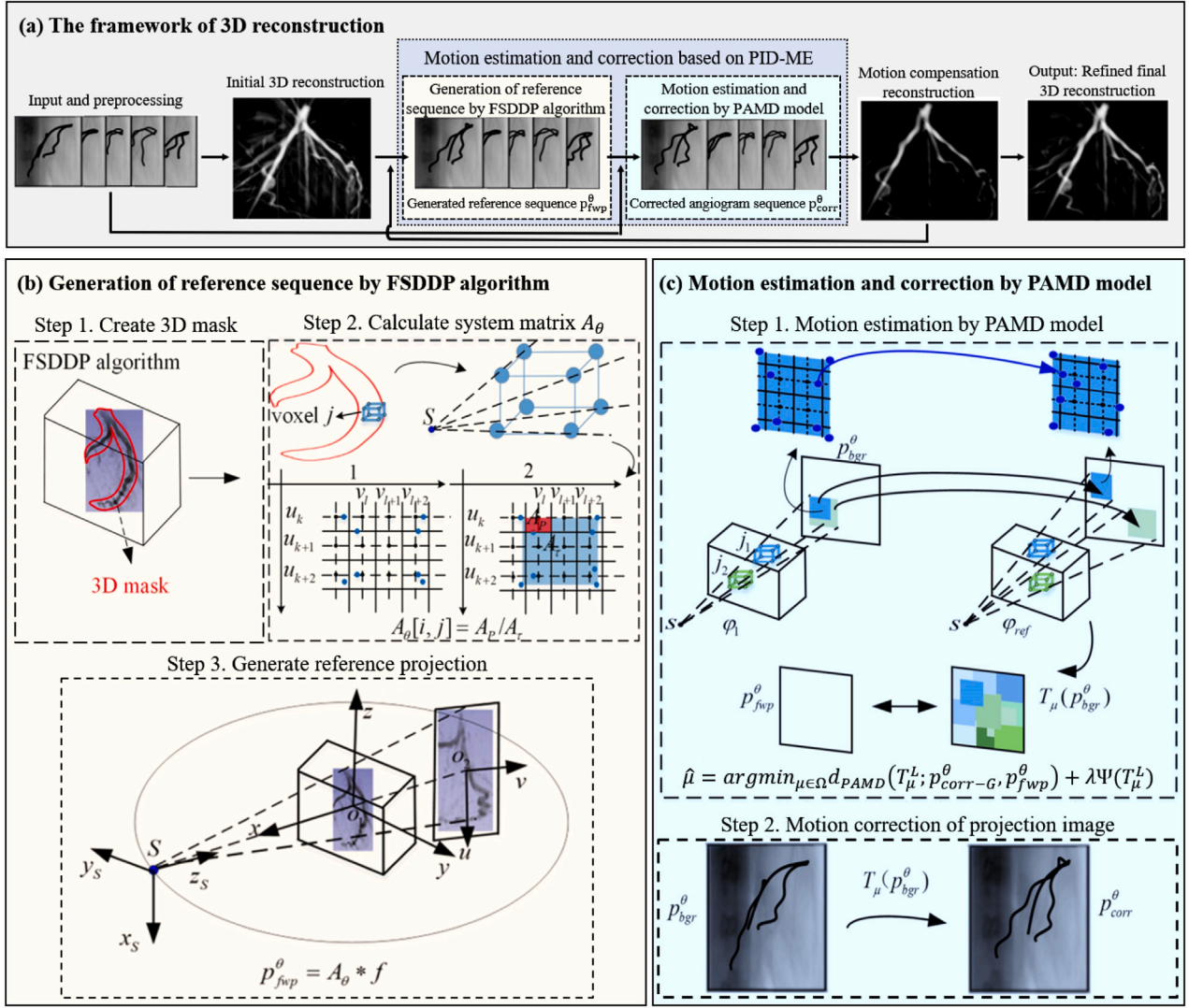


**Fig. 2.** Overview of the 3D reconstruction framework of our 2D-PID-MCR method. (a) The workflow for 3D reconstruction. (b) The three steps for generation of reference sequence by using FSDDP algorithm. (c) The steps for motion estimation and correction by using PAMD model. The step 1 of motion estimation by PAMD model includes three parts: algorithm of PAMD model, geometric transformation model, and optimization.

### 3.3. Generation of reference sequence by FSDDP algorithm

The algorithm of generating the reference forward projection sequence is shown in Fig. 2b. Steps 1 and 2 are used to calculate the system matrix  $A_\theta$  of the imaging system model. Then, as shown in Step 3 of Fig. 2b, the reference projection sequence images  $p_{fwp}^\theta$  ( $\theta = \theta_1, \dots, \theta_K$ ) can be calculated as:

$$p_{fwp}^\theta = A_\theta \times f_{\varphi_{ref}}^{(n)} \quad (2)$$

where  $f_{\varphi_{ref}}^{(n)}$  is the current 3D reconstructed image.  $A_\theta$  has  $N_u \times N_v$  rows and  $N_x \times N_y \times N_z$  columns, where  $N_u$  and  $N_v$  are the resolution of the projection image,  $N_x, N_y$ , and  $N_z$  are the resolution of the reconstruction image.

We propose a FSDDP algorithm to calculate the system matrix  $A_\theta$  faster. The proposed algorithm can generate the reference projection sequence accurately and efficiently. Here, we review the SDDP algorithm briefly. The SDDP algorithm [30] proved to be a simple and accurate method to calculate the system matrix  $A_\theta$  (at the acquisition angle  $\theta$ ) for the X-ray CBCT imaging system. There are three main steps to calculate the coefficient  $a_\theta[i, j]$  ( $i = 1, \dots, N_u \times N_v; j = 1, \dots, N_x \times N_y \times N_z$ ) of  $A_\theta$ : (a) Calculate the projection points of the 8 vertices of  $f_j$ , which is the  $j$ th voxel of the defined 3D reconstructed volume  $f$ .

(b) Draw the smallest rectangle ( $A_r$ ) that contains the 8 projection points, as shown in Step 2 of Fig. 2b. ( $A_r$ ) is shown in the blue rectangle. We suppose that the probability of a photon passing through the voxel  $f_j$  and being detected within the blue rectangular surface is 1.

(c) Calculate the overlapping surface ( $A_p$ ) of the rectangle  $A_r$  and the  $i$ th pixel of the defined projection image (the coordinate of the pixel is  $(u_k, v_l)$ ).  $A_p$  is shown in the red rectangle in Step 2 of Fig. 2b. Then, the coefficient can be calculated as  $a_\theta[i, j] = A_p/A_r$ .

The proposed FSDDP algorithm can accelerate the original SDDP algorithm by reducing the useless and repetitive computation. Firstly, we apply Otsu threshold algorithm [31] to segment the current reconstructed 3D image  $f_{\varphi_{ref}}^{(n)}$ . The generated 3D binary mask can contain all the voxels of the 3D coronary structure (Step 1 of Fig. 2b). Secondly, we combine the SDDP algorithm [30] with the generated 3D mask to calculate the system matrix  $A_\theta$  ( $\theta = \theta_1, \dots, \theta_K$ ).  $f_{\varphi_{ref}}^{mask}$  is the 3D volume of the generated 3D mask. Now, we can just consider the voxels inside  $f_{\varphi_{ref}}^{mask}$ , which occupies a small space of the original volume  $f$ . We just need to calculate the coefficient  $a_\theta[i, j]$  ( $i = 1, \dots, N_u \times N_v; f_{\varphi_{ref}} - j \in f_{\varphi_{ref}}^{mask}$ ) of  $A_\theta$ . Other components of  $a_\theta[i, j]$  ( $f_{\varphi_{ref}} - j \notin f_{\varphi_{ref}}^{mask}$ ) can be set as 0 (Step 2 of Fig. 2b).

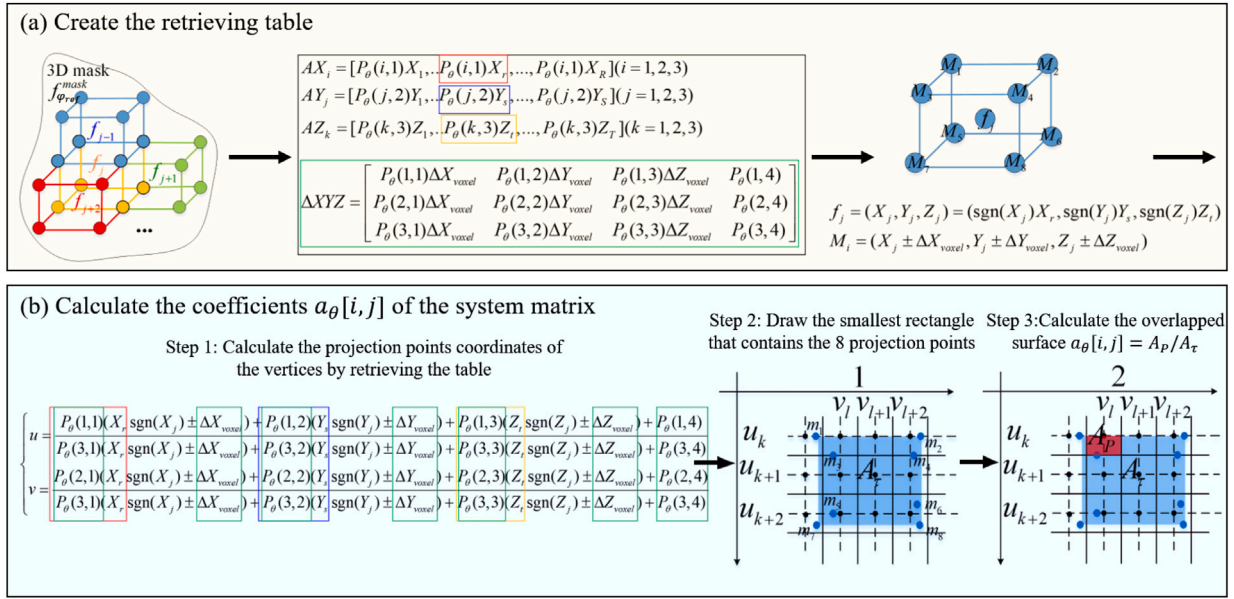


Fig. 3. The detailed illustration of calculating the system matrix for the FSDDP algorithm. (a) Creating the retrieving table according to the 3D binary mask. (b) The three steps for calculating the coefficients  $a_\theta[i, j]$  of the system matrix.

We focus on the modification of the original step (a) to accelerate the calculation of the system matrix  $A_\theta$  further. We exploit the characteristics of the central projection and the symmetric feature of the 3D volume space to reduce the repetitive computation. We suppose that  $f_{\varphi_{ref-j}}$  is one voxel belonging to  $f_{\varphi_{ref}}^{mask}$ ,  $M = (X, Y, Z, 1)^T$  is one of the vertices of  $f_{\varphi_{ref-j}}$ . The projection point  $m = (u, v, 1)^T$  of  $M$  can be calculated by the central projection formula as:

$$sm = P_\theta M \quad (3)$$

where  $P_\theta$  is a projection matrix at angle  $\theta$ . Generally,  $P_\theta$  is a matrix with 3 rows and 4 columns and must be calculated by the calibrated or ideal acquisition geometry parameters [32,33]. Calibration work will not be discussed in this study. Let us expand the central projection formula (3) as:

$$u = \frac{P_\theta(1, 1)X + P_\theta(1, 2)Y + P_\theta(1, 3)Z + P_\theta(1, 4)}{P_\theta(3, 1)X + P_\theta(3, 2)Y + P_\theta(3, 3)Z + P_\theta(3, 4)} \quad (4a)$$

$$v = \frac{P_\theta(2, 1)X + P_\theta(2, 2)Y + P_\theta(2, 3)Z + P_\theta(2, 4)}{P_\theta(3, 1)X + P_\theta(3, 2)Y + P_\theta(3, 3)Z + P_\theta(3, 4)} \quad (4b)$$

where  $P_\theta(k, l)(k = 1, 2, 3; l = 1, 2, 3, 4)$  are the components of the projection matrix. Observing the formula (4), we find that the numerator and denominator of  $u, v$  are the sum of 4 terms. As shown in Fig. 3, for example, the voxel  $f_{\varphi_{ref-j}}$  and its neighboring voxels have many coincident vertices. When we deal with the voxels one by one, we will calculate the projection of the coincident vertices repetitively. Therefore, we create a retrieving table to reduce the large amount of repetitive multiplications.  $X_j \in [X_1, \dots, X_r, \dots, X_R]$ ,  $Y_j \in [Y_1, \dots, Y_s, \dots, Y_S]$ ,  $Z_j \in [Z_1, \dots, Z_t, \dots, Z_T]$  are the absolute values of all the possible voxels coordinates components of  $f_{\varphi_{ref}}^{mask}$  (from smallest to largest).  $\Delta X_{voxel}, \Delta Y_{voxel}, \Delta Z_{voxel}$  are half of the voxel size:

$$AX_i = [P_\theta(i, 1)X_1, \dots, P_\theta(i, 1)X_r, \dots, P_\theta(i, 1)X_R](i = 1, 2, 3) \quad (5a)$$

$$AY_j = [P_\theta(j, 2)Y_1, \dots, P_\theta(j, 2)Y_s, \dots, P_\theta(j, 2)Y_S](j = 1, 2, 3) \quad (5b)$$

$$AZ_k = [P_\theta(k, 3)Z_1, \dots, P_\theta(k, 3)Z_t, \dots, P_\theta(k, 3)Z_T](k = 1, 2, 3) \quad (5c)$$

According to formula (4), the retrieving table includes nine one-dimensional arrays and one matrix with 3 rows and 4 columns as:

$$\Delta XYZ = \begin{bmatrix} P_\theta(1, 1)\Delta X_{voxel} & P_\theta(1, 2)\Delta Y_{voxel} & P_\theta(1, 3)\Delta Z_{voxel} & P_\theta(1, 4) \\ P_\theta(2, 1)\Delta X_{voxel} & P_\theta(2, 2)\Delta Y_{voxel} & P_\theta(2, 3)\Delta Z_{voxel} & P_\theta(2, 4) \\ P_\theta(3, 1)\Delta X_{voxel} & P_\theta(3, 2)\Delta Y_{voxel} & P_\theta(3, 3)\Delta Z_{voxel} & P_\theta(3, 4) \end{bmatrix} \quad (6)$$

The proposed FSDDP algorithm can be described as follows: First, generate a 3D binary mask  $f_{\varphi_{ref}}^{mask}$  that can contain all the voxels of the 3D coronary structure. Second, create a retrieving table according to  $f_{\varphi_{ref}}^{mask}$ , as shown in Fig. 3a. Third, calculate the coefficients  $a_\theta[i, j](i = 1, \dots, N_u \times N_v; f_{\varphi_{ref-j}} \in f_{\varphi_{ref}}^{mask})$  of  $A_\theta$ , as shown in Fig. 3b. There are three steps. Step 1 is to calculate the projection points coordinates of the 8 vertices of  $f_{\varphi_{ref-j}}$  ( $f_{\varphi_{ref-j}} \in f_{\varphi_{ref}}^{mask}$ ) by retrieving the created table. We assume that there is the coordinate of the voxel  $f_{\varphi_{ref-j}} = (X_j, Y_j, Z_j) = (\text{sgn}(X_j)X_r, \text{sgn}(Y_j)Y_s, \text{sgn}(Z_j)Z_t)$ , where  $\text{sgn}$  is the sign function,  $X_r, Y_s, Z_t$  are the absolute values of  $X_j, Y_j, Z_j$ . The coordinates of the 8 vertices  $M_k(k = 1, \dots, 8)$  of  $f_{\varphi_{ref-j}}$  can be represented as  $M_k = (X_j \pm \Delta X_{voxel}, Y_j \pm \Delta Y_{voxel}, Z_j \pm \Delta Z_{voxel})$ . Therefore, the projection point  $m_k$  of the 8 vertices can be calculated by retrieving the created table. Concretely, we apply the formula (4) to calculate the projection point  $m_k(k = 1, \dots, 8)$ . Then, we have:

$$u = \frac{P_\theta(1, 1)(X_j \pm \Delta X_{voxel}) + P_\theta(1, 2)(Y_j \pm \Delta Y_{voxel}) + P_\theta(1, 3)(Z_j \pm \Delta Z_{voxel}) + P_\theta(1, 4)}{P_\theta(3, 1)(X_j \pm \Delta X_{voxel}) + P_\theta(3, 2)(Y_j \pm \Delta Y_{voxel}) + P_\theta(3, 3)(Z_j \pm \Delta Z_{voxel}) + P_\theta(3, 4)} \quad (7)$$

$$v = \frac{P_\theta(2, 1)(X_j \pm \Delta X_{voxel}) + P_\theta(2, 2)(Y_j \pm \Delta Y_{voxel}) + P_\theta(2, 3)(Z_j \pm \Delta Z_{voxel}) + P_\theta(2, 4)}{P_\theta(3, 1)(X_j \pm \Delta X_{voxel}) + P_\theta(3, 2)(Y_j \pm \Delta Y_{voxel}) + P_\theta(3, 3)(Z_j \pm \Delta Z_{voxel}) + P_\theta(3, 4)}$$

where  $P_\theta(l, 1)X_r(l = 1, 2, 3)$  can be retrieved by the  $r$ -th component of  $AX_i$ .  $P_\theta(m, 2)Y_s(m = 1, 2, 3)$  and  $P_\theta(n, 3)Z_t(n = 1, 2, 3)$  can be retrieved in a similar way.  $P_\theta(l, 1)\Delta X_{voxel}$ ,  $P_\theta(m, 2)\Delta Y_{voxel}$ ,  $P_\theta(n, 3)\Delta Z_{voxel}$ , and  $P_\theta(p, 4)(p = 1, 2, 3)$  can be retrieved by  $\Delta XYZ$ . In Fig. 3b, steps 2 and 3 are the same as steps (b) and (c) of the SDDP algorithm. Fourth: Set the coefficients  $a_\theta[i, j](i = 1, \dots, N_u \times N_v; f_{\varphi_{ref-j}} \notin f_{\varphi_{ref}}^{mask})$  to be 0.

### 3.4. Motion estimation by PAMD model

We propose a PAMD model for the precise pixel motion estimation from the acquired projection  $p_{bgr}^\theta$  to the reference pixel projection  $p_{fwp}^\theta$ . We develop a projection information disentanglement-based registration framework for the motion estimation of projection data. For the similarity measures of the objective function, average minimal distance

measures in [34] are shown to be characterized by smooth distance surfaces with significantly fewer local minima than the commonly used intensity-based measures. We develop these average minimal distance measures further to apply to our specific problem. We refer to the new similarity measures as the PAMD measure model. Then, we perform affine transformation to replace one points in one space to another. The stochastic gradient descent optimization methods are used for local iterative optimization.

### 3.4.1. Projective average minimal distance model

Images are considered as fuzzy sets in this model. A fuzzy set  $S$  on a reference set  $X_S$  is a set of ordered pairs,  $S = \{(x, \mu_S(x)) : x \in X_S\}$ , where  $\mu_S : X_S \rightarrow [0,1]$  is the membership function of  $S$ . A gray-scale image can be directly interpreted as a spatial fuzzy set by rescaling the valid intensity range to  $[0,1]$ . The images to be registered can be interpreted as fuzzy sets defined on a reference set which is the image domain. Given a similarity measure  $d$  and a set of valid geometric transformations  $\Omega$ , intensity-based registration of two images  $p_{bgr}^\theta$  (floating) and  $p_{fwp}^\theta$  (reference) can be formulated as the optimization problem:

$$\hat{\mu} = \underset{\mu \in \Omega}{\operatorname{argmin}} d_{PAMD}(T_\mu; p_{bgr}^\theta, p_{fwp}^\theta) \quad (8)$$

$T_\mu$  denotes a valid transform from image  $p_{bgr}^\theta$  to the reference image  $p_{fwp}^\theta$ .

We utilize the similarity measure of average minimal distance (AMD)  $\bar{d}_{\alpha AMD}^R$  for image registration [34]:

$$d_{PAMD}(T_\mu; p_{bgr}^\theta, p_{fwp}^\theta) = \bar{d}_{\alpha AMD}^R(p_{bgr}^\theta, p_{fwp}^\theta; T_\mu, \omega_{bgr}^\theta, M_{fwp}^\theta) \quad (9)$$

Given fuzzy set  $p_{bgr}^\theta$  on the reference set  $X_{bgr}^\theta$ , fuzzy set  $p_{fwp}^\theta$  on the reference set  $X_{fwp}^\theta$ , weight functions  $\omega_{bgr}^\theta : X_{bgr}^\theta \rightarrow R \geq 0$  and crisp subset (mask)  $M_{fwp}^\theta \subset R^n$ ,  $\bar{d}_{\alpha AMD}^R$  is parameterized by a transformation  $T_\mu : R^n \rightarrow R^n$  and defined as:

$$\bar{d}_{\alpha AMD}^R(p_{bgr}^\theta, p_{fwp}^\theta) = \frac{\sum_{y \in \hat{Y}} \omega_{bgr}^\theta(y) \bar{d}^\alpha(T_\mu(p_{bgr}^\theta)(y), p_{fwp}^\theta(y))}{\sum_{y \in \hat{Y}} \omega_{bgr}^\theta(y)} \quad (10)$$

with  $\hat{Y} = \{y : y \in M_{fwp}^\theta\}$ . == The fuzzy point-to-set bidirectional distance  $\bar{d}^\alpha$  between fuzzy point  $y$  and a fuzzy set  $S$  is defined as:

$$\bar{d}^\alpha(y, S) = d^\alpha(y, S) + \bar{d}^\alpha(y, S) \quad (11)$$

The fuzzy point-to-set distance  $d^\alpha$  is defined as:

$$d^\alpha(y, S) = \int_0^{h_y} d_E(y, S^\alpha) d\alpha \quad (12)$$

where  $h_y = \mu_p(y)$ ,  $y \in X_S$ ,  $d_E$  is a point-to-set distance defined on crisp sets and the formula is  $d_E(y, S^\alpha) = \inf_{s \in S^\alpha} d_E(y, s)$ . The point-to-point distance  $d(y, x)$  is the Euclidean distance.  $S^\alpha$  is the  $\alpha$ -cut of the fuzzy set  $S$  with the definition as:

$$S^\alpha = \{x \in X_S : \mu_S(x) \geq \alpha\} \quad (13)$$

$\bar{d}^\alpha(y, S) = d^\alpha(\bar{y}, \bar{S})$  is the complement distance of  $d^\alpha(y, S)$ . The complement of a fuzzy set  $S$  is  $\bar{S} = \{(x, 1 - \mu_S(x)) : x \in X_S\}$ .

Next, as the projection image domain is composed of a lot of overlapping projection pixels, we rewrite the formula (10) and recalculate the fuzzy sets of  $T_\mu(p_{bgr}^\theta)$  by projection information disentanglement. The main strategy is based on the proposed FSDDP algorithm to calculate the transformed projection domain of each voxel and compose the transformed projection image. As shown in Fig. 2c, we have the following steps: First, as described in 3.3, we reconstruct a rough 3D image  $f_\varphi$  at current cardiac phase  $\varphi(\theta)$  and generate a 3D mask  $V^{mask}$  of  $f_\varphi$ . Then, recalculate the fuzzy sets of  $T_\mu(p_{bgr}^\theta)$  as the following three steps:

(a) Calculate the projection domain  $A_{j\tau}$  of each voxel  $j$  inside  $V^{mask}$ . For each voxel  $j(j = 1, \dots, N)$  inside the mask, we calculate the projection points of the 8 vertices of  $j$ , as shown in Fig. 3a and Step

1 of Fig. 3b. We assume that the projection points of the 8 vertices are  $p_j^{vi}(i = 1, \dots, 8)$ . As described in 3.3, the locations of  $p_j^{vi}$  decides the projection domain  $A_{j\tau}$  of voxel  $j$ . Then, we can find the projection pixels  $i_{A_{j\tau}}$  belonging to  $A_{j\tau}$ . The contribution of voxel  $j$  to pixel  $i_{A_{j\tau}}$  is  $a_\theta[i_{A_{j\tau}}, j]$  which can be calculated by FSDDP.

(b) Calculate the transformed projection domain  $A_{j\tau}^t$  corresponding to  $A_{j\tau}$ . The locations of  $p_j^{vi}$  will be transformed to the new locations  $p_j^{vit} = T_\mu(p_j^{vi})$  resulting from the cardiac motion. The locations of  $p_j^{vit}$  decide the new projection domain  $A_{j\tau}^t$ . Then, we find all the projection pixels  $i_{A_{j\tau}^t}$  that belongs to  $A_{j\tau}^t$  and calculate the contribution  $a_\theta^t[i_{A_{j\tau}^t}, j]$  of voxel  $j$  to pixel  $i_{A_{j\tau}^t}$ . The intensity value component of pixel  $i_{A_{j\tau}^t}$  contributed by voxel  $j$  can be calculated as:

$$I(i_{A_{j\tau}^t}) = \sum_{i_{A_{j\tau}^t} \in A_{j\tau}^t} \frac{\mu_{p_{bgr}^\theta}(i_{A_{j\tau}^t}) f_j^{current}}{\sum_{j=1}^N a_\theta[i_{A_{j\tau}^t}, j] f_j^{current}} a_\theta^t[i_{A_{j\tau}^t}, j] / N_i \quad (14)$$

where  $\mu_{p_{bgr}^\theta}$  is the intensity value of pixel  $i_{A_{j\tau}^t}$  of image  $p_{bgr}^\theta$ ,  $f_j^{current}$  is intensity value of voxel  $j$  of the current 3D reconstruction  $f$ , and  $N_i$  is the number of pixels belonging to  $A_{j\tau}^t$ .

(c) Compose the transformed projection image  $p_{tbgr}^\theta$ .  $\mu_{p_{tbgr}^\theta}(i)$  is the intensity value of pixel  $i$  of  $p_{tbgr}^\theta$ , which can be calculated as:

$$\mu_{p_{tbgr}^\theta}(i) = \begin{cases} \sum_{j=1}^N I(i_{A_{j\tau}^t}) & i \in A_{j\tau}^t \\ 0, & i \notin A_{j\tau}^t \end{cases} \quad (15)$$

The Eq. (10) can be rewritten as:

$$\bar{d}_{\alpha AMD}^R(p_{bgr}^\theta, p_{fwp}^\theta) = \frac{\sum_{x \in \hat{X}} \omega_{p_{bgr}^\theta}^\theta(x) \bar{d}^\alpha(T_\mu(p_{bgr}^\theta)(x), p_{fwp}^\theta)}{\sum_{x \in \hat{X}} \omega_{p_{bgr}^\theta}^\theta(x)} \quad (16)$$

where

$$T_\mu(p_{bgr}^\theta) = p_{tbgr}^\theta \quad (17a)$$

$$p_{tbgr}^\theta = \left\{ (x, \mu_{p_{tbgr}^\theta}(x)) : x \in X_{p_{tbgr}^\theta}^\theta \right\} \quad (17b)$$

$$\hat{X} = \left\{ x : x \in X_{p_{tbgr}^\theta}^\theta \wedge x \in M_{p_{fwp}^\theta}^\theta \right\} \quad (17c)$$

### 3.4.2. Geometric transformation model

We apply affine transformation  $T_\mu^G$  to model the global geometric transformation from acquired projection  $p_{bgr}^\theta$  to the reference projection  $p_{fwp}^\theta$ . The affine transformation model  $T_\mu^G$  has the following definition [35]:

$$T_\mu^G = Hx + T \quad (18)$$

where  $H$  indicates the linear transformation,  $T$  is the translation.  $\mu = [h_{11}, h_{12}, h_{21}, h_{22}, t_u, t_v]$ , where  $h_{ij}(i = 1, 2; j = 1, 2)$  are the components of matrix  $H$ ,  $t_u, t_v$  are the components of the vector  $T$ .

We apply B-spline transformation  $T_\mu^L$  to model the local deformation [35]. The optimization problem (formula (8)) can be rewritten as:

$$\hat{\mu} = \underset{\mu \in \Omega}{\operatorname{argmin}} d_{PAMD}(T_\mu^L, p_{corr-G}^\theta, p_{fwp}^\theta) + \lambda \Psi(T_\mu^L) \quad (19)$$

where  $\Psi(T_\mu^L)$  is the regularization term to constraint B-spline transformation.  $\lambda$  denotes the regularization parameter. The B-spline model  $T_\mu^L$  has the following definition:

$$T_\mu^L(x) = x + \sum_{x_k \in N_x} \mu_k \beta^3((x - x_k)/\sigma) \quad (20)$$

where  $x_k$  denotes the control knots,  $\beta^3$  denotes the cubic B-spline,  $\sigma$  denotes the interval between neighboring knots, and  $\mu_k$  denotes the B-spline coefficients at the knot  $x_k$ .  $\mu = [\mu_1, \mu_2, \dots, \mu_M]$ , where  $M$  is the total number of knots in the 2D image domain. We adopt the regularization term in [36] to penalize an unacceptably large coefficient difference between neighboring knots. The definition of  $\Psi(T_\mu^L)$  is as follows:

$$\Psi(T_\mu^L) = \sum_k \sum_{j \in N_k} \|\mu_k - \mu_j\|_2^2 \quad (21)$$



where  $N_k$  denotes a neighborhood of knot  $\mu_k$ .

### 3.4.3. Optimization

We adopt stochastic gradient descent optimization methods to solve the optimization problems stated in formulas (8) and (19). As we know, the gradient of the objective function is required. For the local transformation, the gradient of the regularization term  $\nabla\mathcal{P}$  can be easily derived from formula (21). The difficulty for two kinds of transformation is deriving the gradient of the proposed PAMD distance measures  $\nabla d_{PAMD} = [\frac{\partial d_{PAMD}}{\partial \mu_1}, \frac{\partial d_{PAMD}}{\partial \mu_2}, \dots, \frac{\partial d_{PAMD}}{\partial \mu_M}]^T$  ( $M$  is 6 for the global affine transformation and equals to the number of knots for the local B-spline transformation). Observing the formula (9) to (13), we can find that the partial derivative  $\frac{\partial d_{PAMD}}{\partial \mu_m}$  ( $m = 1, \dots, M$ ) is easy to be derived as long as  $\frac{\partial d^\alpha}{\partial \mu_m}$  is obtained. The transformation is not a simple pixel-to-pixel mapping so that  $\frac{\partial d^\alpha}{\partial \mu_m}$  has a more complex derivation.

As shown in formula (12), the distance  $d^\alpha$  has three implicit functions of parameters  $\mu$ . They are  $y_u, y_v$  and  $h_y$ , where  $y_u$  and  $y_v$  indicate the coordinate component of pixel  $y$  inside the transformed projection domain  $A_{j\tau}^t$ . Then,  $\partial d^\alpha / \partial \mu_m$  can be expressed as:

$$\frac{\partial d^\alpha}{\partial \mu_m} = \frac{\partial d^\alpha}{\partial y_u} \frac{\partial y_u}{\partial \mu_m} + \frac{\partial d^\alpha}{\partial y_v} \frac{\partial y_v}{\partial \mu_m} + \frac{\partial d^\alpha}{\partial h_y} \frac{\partial h_y}{\partial \mu_m} \quad (22)$$

where  $\frac{\partial d^\alpha}{\partial h_y}$  can be obtained by the formula of the derivative of the definite integral, as:

$$\frac{\partial d^\alpha}{\partial h_y} = d_E(y, S^{h_y}) \quad (23)$$

Then,  $\frac{\partial d^\alpha}{\partial y_u}$  can be calculated as ( $\frac{\partial d^\alpha}{\partial y_v}$  has the similar derivation):

$$\frac{\partial d^\alpha}{\partial y_u} = \int_0^{h_y} \frac{\partial d_E}{\partial y_u} d\alpha \quad (24)$$

We rewrite the definition of  $d_E(y, S^\alpha)$  to calculate  $\frac{\partial d_E}{\partial y_u}$  as:

$$\begin{aligned} d_E(y, S^\alpha) &= \inf_{s_i \in S^\alpha} d_E(y, s_i) \\ &= \min(d_E(y, s_1), d_E(y, s_2), \dots, d_E(y, s_k)) \end{aligned} \quad (25)$$

Next, we focus on deriving the partial derivative  $\frac{\partial y_u}{\partial \mu_m}$  ( $\frac{\partial y_v}{\partial \mu_m}$  has similar derivation). As described in 3.4.1, the locations of  $p_j^{vit}$  will be transformed to the new locations  $p_j^{vit}$  by  $T_\mu(p_j^{vi})$ . The transformed projection domain  $A_{j\tau}^t$  is determined by  $p_j^{vit}$  ( $i = 1, \dots, 8$ ). The coordinate of the pixels  $y$  inside  $A_{j\tau}^t$  can be calculated as:

$$y_u^{min} = \text{round}(\min(p_{ju}^{v1t}, p_{ju}^{v2t}, \dots, p_{ju}^{v8t})) \quad (26a)$$

$$y_u^{max} = \text{round}(\max(p_{ju}^{v1t}, p_{ju}^{v2t}, \dots, p_{ju}^{v8t})) \quad (26b)$$

$$n_y = y_u^{max} - y_u^{min} + 1 \quad (26c)$$

$$y_u = y_u^{min} + (n - 1), n = 1, 2, \dots, n_y \quad (26d)$$

where the round function rounds a number to an integer value. Then, we have the expression of  $\frac{\partial y_u}{\partial \mu_m}$  as:

$$\frac{\partial y_u}{\partial \mu_m} = \sum_{i=1}^8 \frac{\partial y_u}{\partial p_{ju}^{vit}} \frac{\partial p_{ju}^{vit}}{\partial \mu_m} \quad (27)$$

### 3.5. Motion correction of projection image

We set the gating window  $\omega_2$  equals to the value of  $\omega_1$  for the first iteration and a wider value of  $\omega_2$  for other iterations of MCR. The projection image inside the gating window except for the reference phase should be corrected according to the estimated geometric transformation model  $T_\mu^G, T_\mu^L$ . Firstly, we correct the global geometric deformation to obtain image  $p_{corr-G}^\theta$  by  $T_\mu^G(p_{bgr}^\theta)$ . Then, we correct the local nonlinear geometric deformation to obtain the final corrected projection image  $p_{corr}^\theta$  by  $T_\mu^L(p_{corr-G}^\theta)$ .

**Table 1**

Clinical datasets used for the evaluation.

Dataset	Resolution	Pixel size	SAD	SDD	Angulation	Num. of frames
LCA1	1024 * 1024	0.139	707	1103	120	80
LCA2	1024 * 1024	0.139	721	1103	120	80
LCA3	512 * 512	0.2875	720	1188	70	78
LCA4	512 * 512	0.2875	720	1188	80	92
LCA5	512 * 512	0.2875	720	1188	70	89
LCA6	512 * 512	0.2875	720	1152	120	114
LCA7	512 * 512	0.2875	720	1105	120	108
LCA8	512 * 512	0.2875	720	1172	120	153
LCA9	512 * 512	0.3375	720	1172	120	155
LCA10	512 * 512	0.3375	720	1172	120	170
RCA1, RCA2	1024 * 1024	0.139	690	1103	120	80

## 4. Experimental setup and evaluation methods

### 4.1. Experimental data

#### 4.1.1. Simulated data

The CAVAREV (Cardiac vasculature reconstruction evaluation) platform is a well-established open platform for evaluating the 3D reconstruction of rotational coronary angiography [37]. It features two simulated dynamic rotational projection datasets based on the 4D XCAT numeric phantom with contrasted coronary arteries which were derived from real patient data. The acquisition protocol and calibrated geometries are all from a real-world C-arm system. The simulated acquisition with a 5 s circular short scan trajectory covers 200° angulation and yields a 2D rotational angiography sequence of 133 projection images. Each projection image has a size of 960 \* 960 pixels and an isotropic pixel size of 0.32 mm. The reconstructed 3D volume has a size of 196 \* 196 \* 196 voxels and an isotropic voxel size of 0.5 mm. The first dataset  $D_1$  only contains a continuous periodic cardiac motion without respiratory and other motions. The second dataset  $D_2$  contains periodic cardiac motion and additional respiratory motion. In this study, we consider only the case without respiratory and other motions, and adopt dataset  $D_1$  for the experiments.

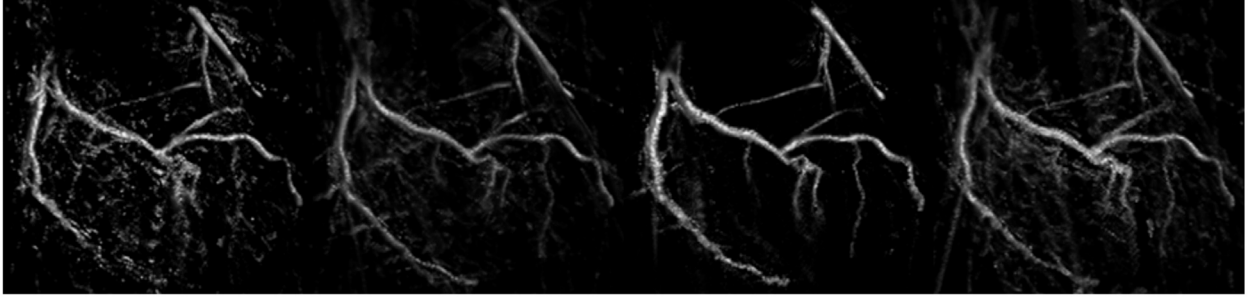
#### 4.1.2. Clinical data

A total of 12 human clinical datasets are acquired for the evaluation. LCA1 to LCA10 are the rotational angiography sequence of the left coronary artery (LCA). RCA1 and RCA2 are the rotational angiography sequence of the right coronary artery (RCA). LCA1, LCA2, RCA1, RCA2 are acquired on Siemens Zeego C-arm devices (Siemens Healthcare, Germany), other datasets are all acquired on GE C-arm device (GE Healthcare, United States). The datasets have no patient and respiratory motion. We list all the acquisition geometries of each data in Table 1. SAD means the distance from X-ray source to isocenter. SDD means the distance from X-ray source to detector. Angulation represents the angulation coverage of the rotational acquisition. For this study, we simply adopt the ideal geometries recorded in the data. The reconstructed 3D volumes have an isotropic voxel size of 0.5 mm and a volume size of 256 \* 256 \* 256.

### 4.2. Evaluation

For the simulated data, the size of the morphological kernel for top-hat filtering is  $r = 3.85$  mm. While for the clinical data, the sizes of top-hat filtering kernel  $r$  are set to 3.85 mm and 3.15 mm for the projection sequence with the image resolution of 1024 \* 1024 and 512 \* 512 respectively. For both simulated and clinical data, the maximum number of optimization step is set to 400, and the optimization is stopped if the magnitude of the objective function is below  $3 \times 10^{-4}$ . Two iterations of the whole MCR are performed. There are qualitative

(a)



(b)

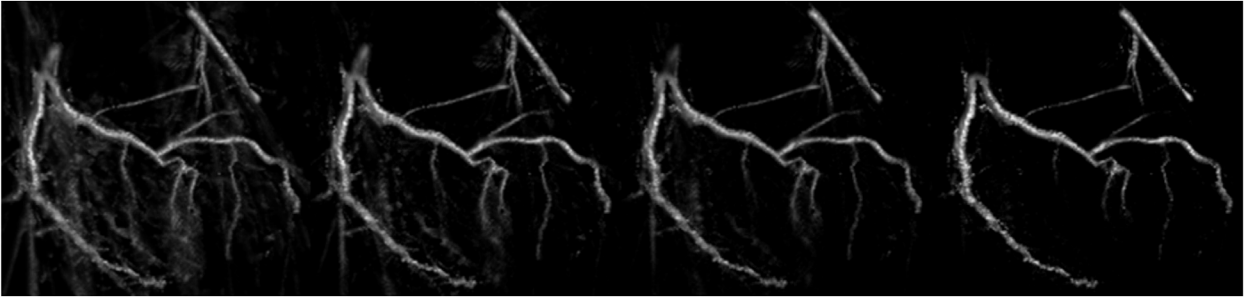
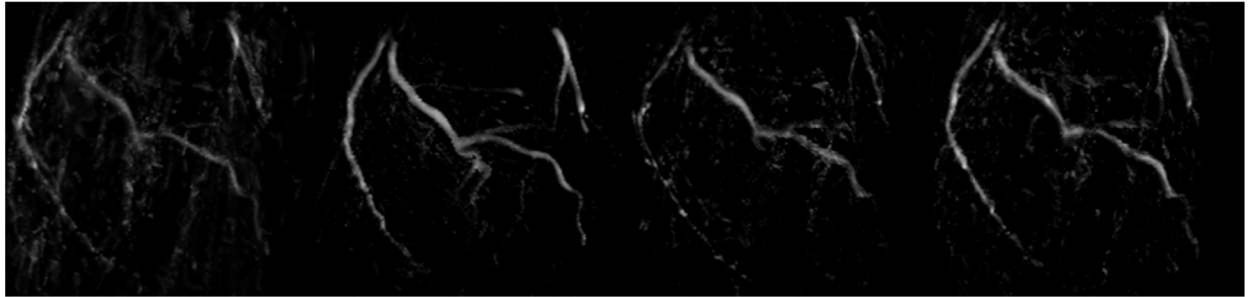


**Fig. 4.** Reconstruction results of CAVAREV dataset of different gating window widths. (a) reconstruction by Schwemmer's algorithm [38]; (b) the proposed reconstruction algorithm. From left to right columns the gating window width  $\omega_2$  of motion compensation is 0.3, 0.45, 0.6, and 0.8.

(a)



(b)

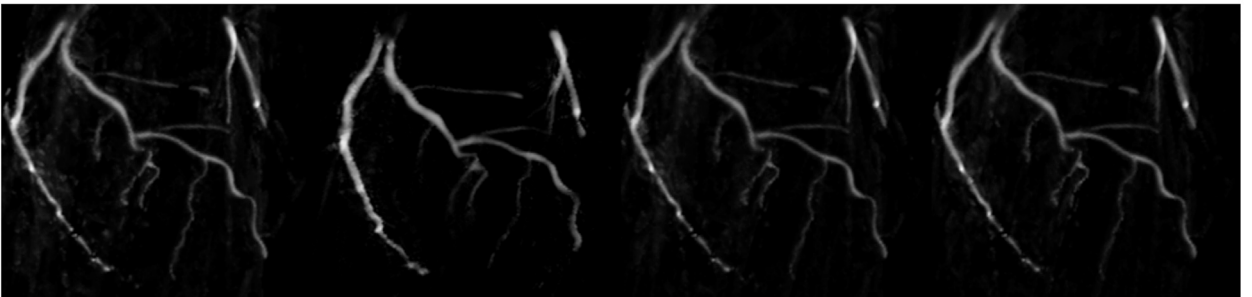


**Fig. 5.** Reconstruction results of CAVAREV dataset of different cardiac phases. (a) reconstruction by Schwemmer's algorithm [38]; (b) the proposed reconstruction algorithm. From left to right columns: the reconstructed phase  $\varphi_{ref}$  equals 0.17, 0.4(ES), 0.6, and 0.8(LD).



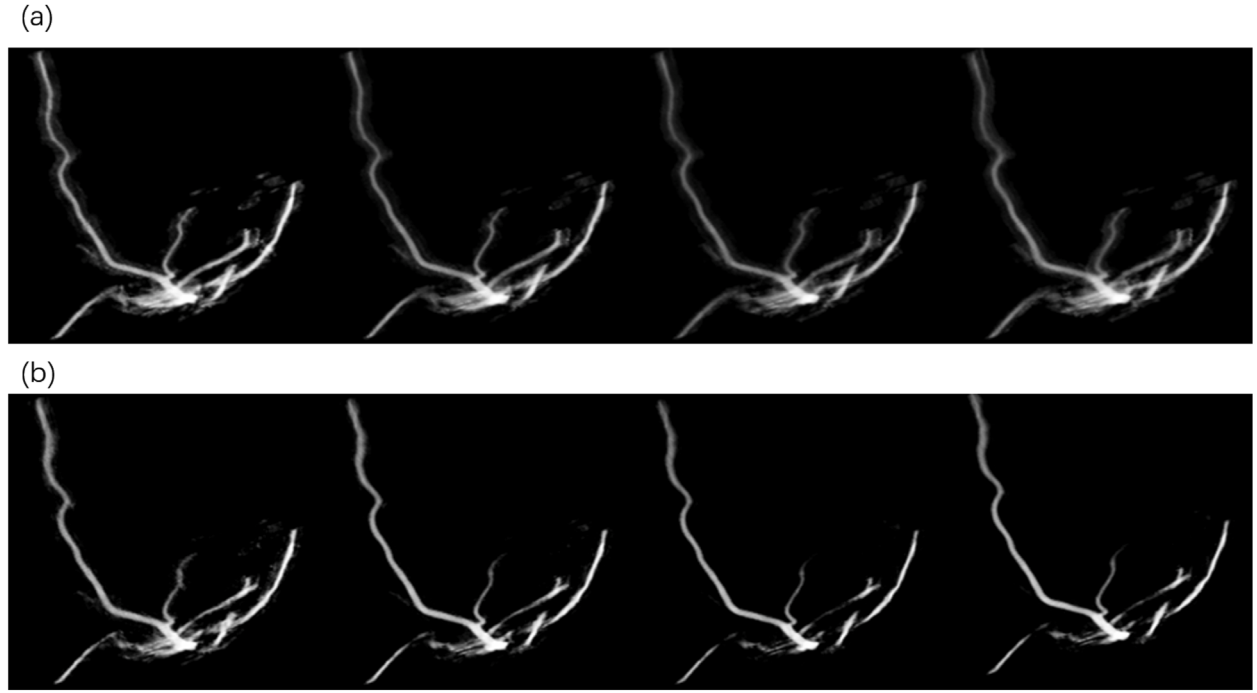


**Fig. 6.** Reconstruction results of clinical data of different gating window widths. (a) reconstruction by Schwemmer's algorithm [38]; (b) reconstruction by the proposed algorithm. From left to right columns: the gating window width  $\omega_2$  of motion compensation is 0.2, 0.4, 0.6, and 0.8.

and quantitative evaluations in this study. We perform the qualitative evaluation visually for both simulated and clinical data. For the quantitative evaluation of the simulated data, we employ the metric provided by CAVAREV platform. For the quantitative evaluation of the clinical data, we have two categories of evaluation metrics, the commonly used metric for image artifacts [38] and vessel sharpness [39], and the proposed forward projection domain metric.

#### 4.2.1. CAVAREV metric

The platform provides two segmentation-based quality measures to assess the 3D and 4D reconstruction quality [38]. The measures are based on the spatial overlap of the vasculature reconstruction with the ground truth. In this study, we use the metric  $Q_{3D}$  provided by CAVAREV platform to evaluate 3D reconstruction quality. The platform provides a series of static binary volume  $f_i^{morph}$  ( $i = 1, 2, \dots, 133$ ) representing the ground truth of the coronary vasculature at all the 133 time points. The reconstructed volume  $f$  will be compared to the ground truth volumes at time point  $i$  to calculate  $Q_i(f)$ :

$$Q_i(f) = \max_{a \in [0, 255]} dsc(f_i^{morph}, T(f, a)) \quad (28)$$

where the reconstruction  $f$  will be rescaled to 8 bit quantization,  $T$  is the threshold function that binarizes  $f$  by the threshold  $a$ :

$$T(f, a)(x) = \begin{cases} 1, & f(x) \geq a \\ 0, & f(x) < a \end{cases} \quad (29)$$

Then,  $dsc$  means Dice similarity coefficient and is defined as:

$$dsc(f_1, f_2) = 2 \frac{\sum_x f_1(x) \cdot f_2(x)}{\sum_x f_1(x) + f_2(x)} \quad (30)$$

The value ranges from 0 (no overlap) to 1 (perfect spatial overlap). As the final result, the metric  $Q_{3D}(f)$  selects the best value over all thresholds and motion phases (time points) and is described as:

$$Q_{3D}(f) = \max_{i \in [1, \dots, 133]} Q_i(f) \quad (31)$$

More details can be found in [37].

#### 4.2.2. Image artifacts and vessel sharpness

There is no ground truth for the clinical data. We use the noise estimator extended by Schwemmer [38] to estimate the image artifacts. This estimator can quantify the motion blur (smoothed out structure) and ghosting artifacts (smooth artifacts in areas without structure) of the reconstructed volume data.

Additionally, we use CoroEval framework [39] to measure the vessel sharpness quantitatively. Firstly, a semi-automatic placement of measurement profile lines is performed for the reconstructed volume. Secondly, the vessel sharpness value at evaluation point  $e_i$  is the mean value of all the profile lines at  $e_i$ . Vessel sharpness of one profile line can be calculated by the measurement algorithm [40]. Finally, the overall mean sharpness is the mean value of all the evaluation points of that vessel segment. The vessel sharpness ranges from 0 to 1, with larger values corresponding to a more definite vessel lumen and indicating superior performance [41]. CoroEval software is available online [39].

#### 4.2.3. Projection domain metric

We propose several projection domain metrics to evaluate the clinical data. In addition to rotational coronary angiography, we also collected CAG sequences of the same patient at multiple angles under the acquisition geometries  $G$ . First of all, we compute the forward projection sequence of the reconstructed volume data by the proposed FSDDP algorithm with the acquisition geometries  $G$ . Secondly, 2D quantitative coronary analysis will be performed both on the CAG and the generated forward projection images. We propose two projection domain metrics  $D(f)$ ,  $L(f)$  that correspond to minimum luminal diameter, vessel length respectively to evaluate the accuracy of the 3D reconstruction of rotational coronary angiography. One experienced cardiologist uses the CoroEval software [39] which also has the 2D quantitative coronary analyses functions to perform the measurements.

As the conventional CAG sequence is acquired at one fixed angle with several cardiac motion cycles, the projection domain metrics should be performed between the forward projection image (FWP) and all the images of the CAG sequence. The two projection domain metrics at one acquisition angle are defined as the minimum evaluation error

by formula (14):

$$D^k(f) = \min_{j \in \{1, \dots, N\}} |D_j^{CAG-k}(f) - D^{FWP-k}(f)| \quad (32a)$$

$$L^k(f) = \min_{j \in \{1, \dots, N\}} |L_j^{CAG-k}(f) - L^{FWP-k}(f)| \quad (32b)$$

where  $D^k(f)$ ,  $L^k(f)$  are the projection domain metrics at angle  $k$ . The number of frames of each CAG sequence is  $N$ .  $D_j^{CAG-k}$  represents the  $j$ th frame image of CAG sequence at angle  $k$ .  $D^{FWP-k}$  means the forward projection image of the 3D reconstruction at angle  $k$ . Finally, the projection domain metrics are defined as the mean of all the acquisition angles (the number of acquisition angles of CAG is  $K$ ) by formula (15):

$$D(f) = [\sum_{k=1}^K D^k(f)]/K \quad (33a)$$

$$L(f) = [\sum_{k=1}^K L^k(f)]/K \quad (33b)$$

## 5. Experimental results and discussion

### 5.1. Qualitative evaluation of 2D-PID-MCR method

We perform two kinds of comparison experiments to evaluate the effectiveness of our 2D-PID-MCR method. One is performed on different gating window widths. The other is on multiple reconstructed phases. We adopt the representative 2D-MCR method proposed by Schwemmer [38] as the comparison algorithm for both for qualitative and quantitative evaluations.

#### 5.1.1. Simulated data

Fig. 4 shows the reconstruction results with different gating window widths  $\omega_2$ . We observe the results row-by-row first. Gradually better results in terms of artifact reduction, homogeneity, and sharpness of the vascular structures can be observed for the proposed method as the gating window width  $\omega_2$  increases. As the comparison, no significant improvement can be found when the gating window width  $\omega_2$  is larger than 0.6. Secondly, we compare the results along columns. The proposed method achieves vascular structures with fewer artifacts, better homogeneity, and sharpness than the reference method, especially for the gating window width  $\omega_2 = 0.6, 0.8$ . The results demonstrate that the proposed method is more powerful to deal with the stronger residual motion inside the larger gating window.

Fig. 5 shows the reconstruction results at different reconstructed phases  $\varphi_{ref}$ . Observing the results along rows, the proposed method obtains a good image quality in terms of artifact level, homogeneity, and sharpness at all the phases while the reference method has the degeneration at the two strong cardiac phases ( $\varphi_{ref} = 0.17, 0.60$ ). Observing the results along columns, the proposed method obtains a better reconstruction image than the reference method. The improvements are more obvious at the two strong motion phases. The results indicate that the proposed method has the stronger capability to deal with the residual motion around the strong motion phase.

#### 5.1.2. Clinical data

We plot the reconstruction results of the clinical datasets LCA1 in Figs. 6 and 7. We can have the consistent conclusion as the simulated data. As shown in Fig. 6, for the reference 2D-MCR method, the increase of gating window width does not further reduce the artifacts and enhance the sharpness of the vasculature structures better when  $\omega_2$  is larger than 0.6. The proposed method could correct the strong residual motion inside a wider gating window and achieve a better result with lower artifacts level (including under-sampling artifacts and motion artifacts). Fig. 7 demonstrates that the proposed method can obtain a good reconstruction even when a non-optimum phase is selected for reconstruction while the reference method has a weak ability for the strong cardiac phases. This capability is very useful in clinical practice as the optimal reconstruction phase is only an estimation value.

### 5.2. Quantitative evaluation of 2D-PID-MCR method

#### 5.2.1. Simulated data

The quantitative evaluation metrics  $Q_{3D}$  of the reconstruction image are listed in Tables 2 and 3. Overall, the value of  $Q_{3D}$  of both methods increases when the gating window width increases. However, the value of  $Q_{3D}$  of the reference method has an increase of 10%, 20%, and 20%, respectively, related to the first reconstruction with  $\omega_2 = 0.3$ . The results indicate that the reference method has no obvious improvement when  $\omega_2$  is larger than 0.6. In comparison,  $Q_{3D}$  of the proposed method has a steady increase of 15%, 30%, and 50%, respectively. Overall,  $Q_{3D}$  of the proposed method has a higher value than the reference one with the same gating window width. The proposed method achieves the best result with  $Q_{3D} = 0.834$  ( $\omega_2 = 0.8$ ) while the reference method obtains the highest value of  $Q_{3D}$  of 0.822 ( $\omega_2 = 0.8$ ). Another hand, the values of  $Q_{3D}$  of the reference method at the two strong motion phases ( $\varphi_{ref} = 0.4, 0.6$ ) are lower than the two rest phases ( $\varphi_{ref} = 0.4, 0.6$ ). As the comparison, the values of  $Q_{3D}$  of the proposed method have no obvious decrease at the two strong motion phases.

These results show that our 2D-PID-MCR method has a stronger capability to deal with the stronger residual motion inside a wider gating window or around the strong cardiac phases. The quantitative results are consistent with the qualitative analysis.

#### 5.2.2. Clinical data

Tables 2 and 3 also list the clinical quantitative evaluation metrics of the reconstruction images. The estimated image artifacts level and vessel sharpness value are carried out as the mean value of all the 12 clinical datasets. For the metric of image artifact level, the proposed reconstruction method yields a reduction of 1%, 2%, 3%, and 4%, respectively, related to the reference method when the gating window width increases by the step of 0.2. The proposed method yields an artifact level reduction of 1%, 2%, 3%, and 4%, respectively, related to the reference one at four different phases. In particular, the proposed method achieves the artifact level of 11, 32 at the two strong phases ( $\varphi_{ref} = 0.4, 0.6$ ) while the reference method has the values of 13, 32. For the metric of vessel sharpness, the proposed method yields an increase of 10%, 20%, 30%, and 40%, respectively, related to the reference method when the gating window width increases. Meanwhile, the proposed method achieves an increase of 10%, 20%, 30%, and 40%, respectively, related to the reference one at different phases. These two metrics indicate that the proposed method corrects the residual motion more effectively and leads to a reconstruction result with fewer motion artifacts and better vessel sharpness.

The projection domain metrics in Tables 2 and 3 indicate that the projection domain metrics have the consistent tendency of image artifacts level and vessel sharpness value. This metric indicates that our 2D-PID-MCR method achieves a 3D reconstruction with more accurate morphological structures of the vessels.

### 5.3. Evaluation PAMD algorithm to disentangle vessel overlapping

Fig. 8 plots the motion correction results of the simulated data in a checkerboard pattern. We select one strong motion phase ( $\varphi = 0.65$ ) to present the results. Comparing (a) and (b), it can be seen that the acquired projection  $p_{bgr}^\theta$  has obvious overlapping structures. The corresponding two separated structures (indicated by the yellow arrows) can be found in (b). As shown in (c), the traditional registration algorithms can correct the displacement of vessel sections effectively. However, it is unable to correct the overlapping structures of the projection data to its corresponding structures effectively. Meanwhile, as shown in (d), the vessel displacement is completely compensated by the proposed motion estimation and correction method, especially for the overlapping structures.

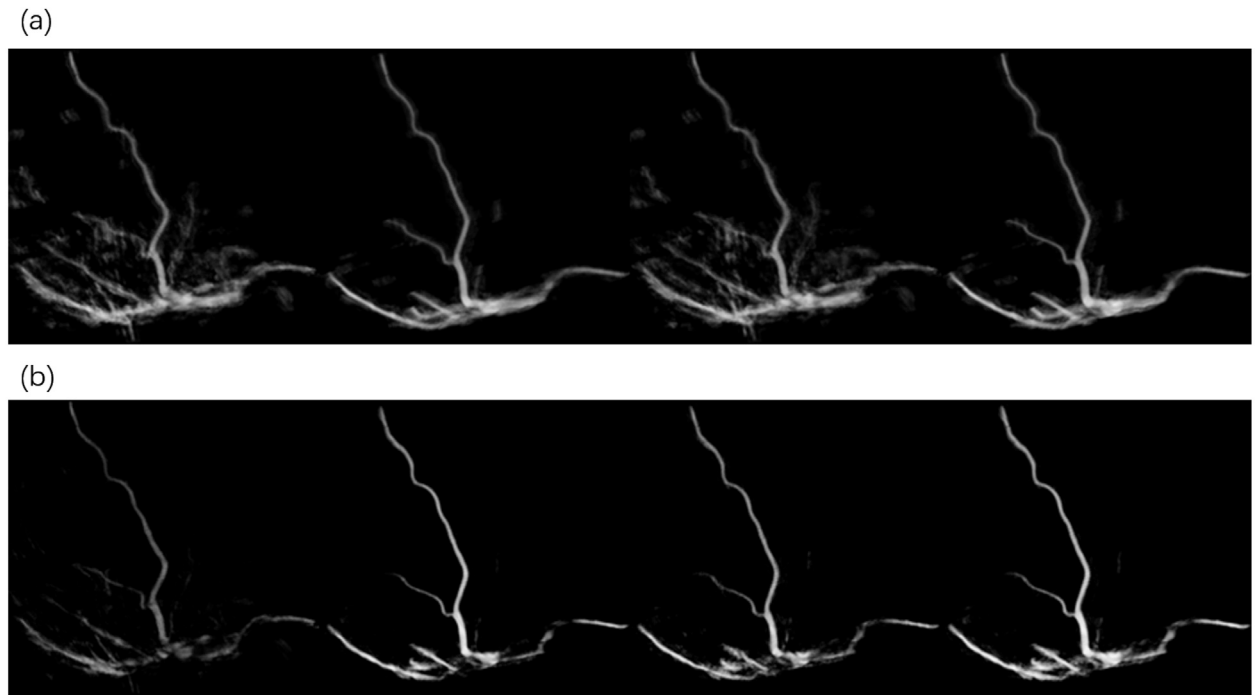


Fig. 7. Reconstruction results of clinical data of different cardiac phases. (a) reconstruction by Schwemmer's algorithm [38]; (b) reconstruction by the proposed algorithm. From left to right columns: the reconstructed phase  $\varphi_{ref} = 0.21, 0.35(\text{ES}), 0.65$ , and  $0.89(\text{LD})$ .

**Table 2**  
Quantitative evaluation of the reconstruction images with different gating window widths.

			Gating window width $\omega_2$			
			0.3/0.2	0.45/0.4	0.6/0.6	0.8/0.8
Simulated dataset	$Q_{3D}$	Ref.	0.758	0.774	0.780	0.770
		Pro.	0.768	0.795	0.823	0.834
Clinical dataset	Artifacts level	Ref.	18.04	16.75	16.43	16.54
		Pro.	17.54	16.33	16.13	16.04
	Vessel sharpness	Ref.	0.486	0.503	0.516	0.501
		Pro.	0.504	0.516	0.524	0.531
	Projection domain metric	Ref.	8.03/7.19/10.11	7.26/6.67/9.18	7.01/6.13/8.11	7.13/6.65/9.16
		Pro.	7.23/7.06/10.02	7.01/6.79/9.01	6.83/6.64/8.91	6.75/6.59/8.62

Ref. means the reference method, Pro. means our 2D-PID-MCR method.

**Table 3**  
Quantitative evaluation of the reconstruction images with different reconstructed phases.

			Reconstructed phase $\varphi_{ref}$			
			0.17/0.21	0.45/0.35	0.6/0.65	0.80/0.89
Simulated dataset	$Q_{3D}$	Ref.	0.761	0.780	0.765	0.792
		Pro.	0.820	0.823	0.819	0.826
Clinical dataset	Artifacts level	Ref.	16.73	16.43	16.70	16.37
		Pro.	16.22	16.13	16.20	16.17
	Vessel sharpness	Ref.	0.477	0.516	0.483	0.510
		Pro.	0.508	0.524	0.515	0.521
	Projection domain metric	Ref.	8.33/7.23/10.31	7.01/6.13/8.11	8.36/7.25/10.41	7.03/6.19/8.01
		Pro.	7.04/6.78/9.21	6.83/6.64/8.91	7.15/6.89/9.35	6.93/6.67/8.79

Ref. means the reference method, Pro. means our 2D-PID-MCR method.

#### 5.4. Evaluation the performance of FSDDP algorithm

In this section, we focus on discussing the proposed FSDDP algorithm. We evaluate the algorithm from three aspects: the computational complexity, the time cost of generating forward projection, and the quantitative metrics of the reconstructed images with different projector algorithms. We take the maximum intensity projector (MIP) algorithm that is widely used in the framework of 2D-MCR methods [38] and the original SDDP algorithm as the reference methods.

We set  $\varphi_{ref} = 0.35$ ,  $\omega_2 = 0.6$  for the simulated data and  $\varphi_{ref} = 0.4$ ,  $\omega_2 = 0.6$  for the clinical data. The results of the clinical data are carried out as the mean values of all the 12 clinical datasets. The proposed FSDDP algorithm can reduce  $8 * 9 = 72$  multiplications for each voxel calculation related to the original SDDP algorithm. The results of the time cost of each projector also indicate that the proposed FSDDP algorithm reduces the computation cost greatly related to the original SDDP algorithm and achieves a bit higher but minor difference with MIP. Another hand, the proposed FSDDP algorithm considers the Cone



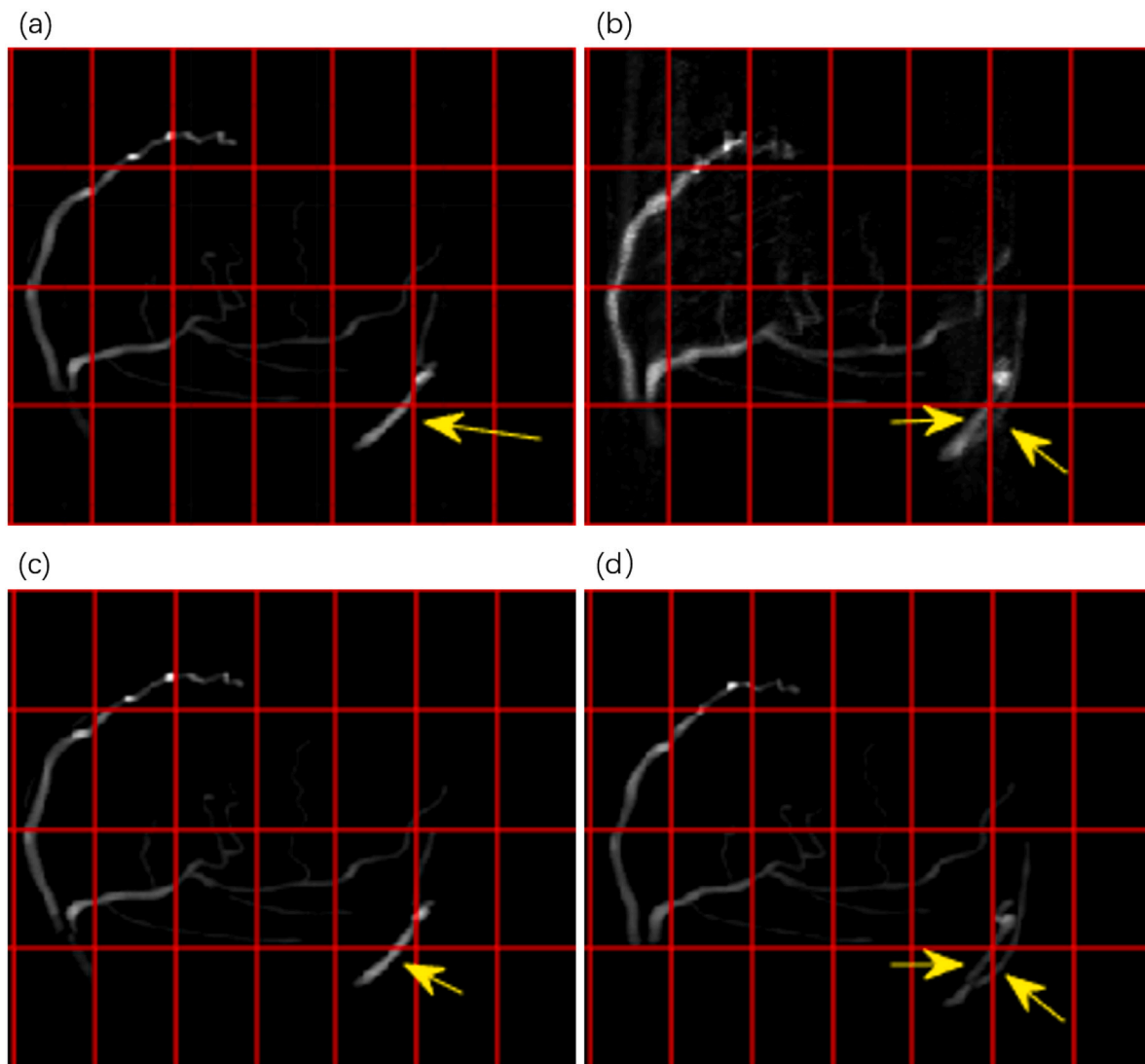


**Fig. 8.** Checkerboard visualization of the motion correction of the simulated data. (a) the acquired projection image  $p_{bgr}^{\theta}$ ; (b) the generated forward projection image  $p_{fw}^{\theta}$ ; (c) the corrected image  $p_{corr}^{\theta}$  by reference method; (d) the corrected image  $p_{corr}^{\theta}$  by proposed method. The projection images correspond to a strong motion phase  $\varphi = 0.65$ .

beam CT imaging principle that is more accurate than MIP algorithm. As a result, the quantitative metric of the reconstruction with FSDDP is 20% higher than the result with the MIP algorithm. Overall, the proposed FSDDP algorithm achieves a better balance between accuracy and real-time performance.

## 6. Conclusions

This study has demonstrated that our 2D-PID-MCR method can perform motion estimation and correction of the overlapping projection pixels for 3D reconstruction of rotational coronary angiography. The results of qualitative and quantitative evaluations on simulated and clinical datasets show that our method effectively overcomes the inherent limitations of existing 2D-MCR methods to disentangle the overlapping projection pixels. Our method outperforms existing 2D-MCR methods in terms of accuracy, robustness, and real-time performance. In the future, we will collect more clinical datasets and further reduce the computational cost by optimizing the motion estimation process.

## Declaration of competing interest

The authors declare that they have no known competing financial interests or personal relationships that could have appeared to influence the work reported in this paper.

## Acknowledgments

This work was supported by the National Natural Science Foundation of China (62101610, 62101606, 62276282, 61976222, U21A20522), the Guangdong Basic and Applied Basic Research Foundation (2022A1515011384), 2020 Li Ka Shing Foundation Cross-Disciplinary Research Grant (2020LKSFG04B), the ERC IMI (101005122), the H2020 (952172), the MRC (MC/PC/21013), the Royal Society (IEC/NSFC/211235), and the UKRI Future Leaders Fellowship (MR/V023799/1).

## References

- [1] J.J. Goldberger, J. Ng, Practical Signal and Image Processing in Clinical Cardiology, Springer, 2010, <http://dx.doi.org/10.1007/978-1-84882-515-4>.
- [2] S. Çimen, A. Gooya, M. Grass, A.F. Frangi, Reconstruction of coronary arteries from X-ray angiography: A review, *Med. Image Anal.* 32 (2016) 46–68.
- [3] H. Zhang, D. Zhang, Z. Gao, H. Zhang, Joint segmentation and quantification of main coronary vessels using dual-branch multi-scale attention network, in: *Medical Image Computing and Computer Assisted Intervention–MICCAI 2021: 24th International Conference, Strasbourg, France, September 27–October 1, 2021, Proceedings, Part I* 24, Springer, 2021, pp. 369–378.
- [4] A.M. Neubauer, J.A. Garcia, J.C. Messenger, E. Hansis, M.S. Kim, A.J. Klein, G.A. Schoonenberg, M. Grass, J.D. Carroll, Clinical feasibility of a fully automated 3D

- reconstruction of rotational coronary X-ray angiograms, *Circ.: Cardiovasc. Interv.* 3 (1) (2010) 71–79.
- [5] J.B. Lee, S.G. Chang, S.Y. Kim, Y.S. Lee, J.K. Ryu, J.Y. Choi, K.S. Kim, J.S. Park, Assessment of three dimensional quantitative coronary analysis by using rotational angiography for measurement of vessel length and diameter, *Int. J. Cardiovasc. Imaging* 28 (7) (2012) 1627–1634.
  - [6] H. Zhang, Z. Gao, D. Zhang, W.K. Hau, H. Zhang, Progressive perception learning for main coronary segmentation in X-ray angiography, *IEEE Trans. Med. Imaging* (2022).
  - [7] C. Rohkohl, G. Lauritsch, A. Nottling, M. Prummer, J. Hornegger, C-arm ct: Reconstruction of dynamic high contrast objects applied to the coronary sinus, in: 2008 IEEE Nuclear Science Symposium Conference Record, IEEE, 2008, pp. 5113–5120, <http://dx.doi.org/10.1109/NSSMIC.2008.4774387>.
  - [8] P. Grangeat, Mathematical framework of cone beam 3D reconstruction via the first derivative of the Radon transform, in: *Mathematical Methods in Tomography*, Springer, 1991, pp. 66–97, <http://dx.doi.org/10.1007/BFb0084509>.
  - [9] E.Y. Sidky, X. Pan, Accurate image reconstruction in circular cone-beam computed tomography by total variation minimization: a preliminary investigation, in: 2006 IEEE Nuclear Science Symposium Conference Record, Vol. 5, IEEE, 2006, pp. 2904–2907, <http://dx.doi.org/10.1109/NSSMIC.2006.356484>.
  - [10] J. Zhou, A. Bousse, G. Yang, J.-J. Bellanger, L. Luo, C. Toumoulin, J.-L. Coatrieux, A blob-based tomographic reconstruction of 3D coronary trees from rotational X-ray angiography, in: *Medical Imaging 2008: Physics of Medical Imaging*, Vol. 6913, International Society for Optics and Photonics, 2008, p. 69132N, <http://dx.doi.org/10.1117/12.769478>.
  - [11] H. Wu, C. Rohkohl, J. Hornegger, Total variation regularization method for 3D rotational coronary angiography, in: *Bildverarbeitung für die Medizin 2011*, Springer, 2011, pp. 434–438, [http://dx.doi.org/10.1007/978-3-642-19335-4\\_89](http://dx.doi.org/10.1007/978-3-642-19335-4_89).
  - [12] Y. Hu, M. Jung, A. Oukili, G. Yang, J.-C. Nunes, J. Fehrenbach, G. Peyré, M. Bedossa, L. Luo, C. Toumoulin, et al., Sparse reconstruction from a limited projection number of the coronary artery tree in X-ray rotational imaging, in: 2012 9th IEEE International Symposium on Biomedical Imaging, ISBI, IEEE, 2012, pp. 804–807, <http://dx.doi.org/10.1109/ISBI.2012.6235670>.
  - [13] E. Hansis, H. Schomberg, K. Erhard, O. Dössel, M. Grass, Four-dimensional cardiac reconstruction from rotational x-ray sequences: first results for 4D coronary angiography, in: *Medical Imaging 2009: Physics of Medical Imaging*, Vol. 7258, International Society for Optics and Photonics, 2009, p. 72580B, <http://dx.doi.org/10.1117/12.811104>.
  - [14] C. Rohkohl, G. Lauritsch, L. Biller, M. Prummer, J. Boese, J. Hornegger, Interventional 4D motion estimation and reconstruction of cardiac vasculature without motion periodicity assumption, *Med. Image Anal.* 14 (5) (2010) 687–694.
  - [15] E. Hansis, J.D. Carroll, D. Schäfer, O. Dössel, M. Grass, High-quality 3-D coronary artery imaging on an interventional C-arm x-ray system, *Med. Phys.* 37 (4) (2010) 1601–1609.
  - [16] C. Schwemmer, C. Rohkohl, G. Lauritsch, K. Müller, J. Hornegger, J. Qi, Opening windows-increasing window size in motion-compensated ecg-gated cardiac vasculature reconstruction, in: *Proc. Int. Meeting Fully Three-Dimensional Image Reconstruction Radiol. Nucl. Med.*, 2013, pp. 50–53.
  - [17] D. Skerl, B. Likar, P. Pernus, A protocol for evaluation of similarity measures for rigid registration, *IEEE Trans. Med. Imaging* 25 (6) (2006) 779–791.
  - [18] F. Maes, A. Collignon, D. Vandermeulen, G. Marchal, P. Suetens, Multimodality image registration by maximization of mutual information, *IEEE Trans. Med. Imaging* 16 (2) (1997) 187–198.
  - [19] C. Blondel, G. Malandain, R. Vaillant, N. Ayache, Reconstruction of coronary arteries from a single rotational X-ray projection sequence, *IEEE Trans. Med. Imaging* 25 (5) (2006) 653–663.
  - [20] A. Bousse, J. Zhou, G. Yang, J.-J. Bellanger, C. Toumoulin, et al., Motion compensated tomography reconstruction of coronary arteries in rotational angiography, *IEEE Trans. Biomed. Eng.* 56 (4) (2008) 1254–1257.
  - [21] R. Zeng, J.A. Fessler, J.M. Balter, Respiratory motion estimation from slowly rotating x-ray projections: Theory and simulation, *Med. Phys.* 32 (4) (2005) 984–991.
  - [22] B. Movassaghi, V. Rasche, R. Florent, M.A. Viergever, W. Niessen, 3D coronary reconstruction from calibrated motion-compensated 2D projections, in: *International Congress Series*, Vol. 1256, Elsevier, 2003, pp. 1079–1084, [http://dx.doi.org/10.1016/S0531-5131\(03\)00399-6](http://dx.doi.org/10.1016/S0531-5131(03)00399-6).
  - [23] E. Hansis, D. Schäfer, O. Dössel, M. Grass, Projection-based motion compensation for gated coronary artery reconstruction from rotational x-ray angiograms, *Phys. Med. Biol.* 53 (14) (2008) 3807.
  - [24] Y. Hu, L. Xie, J.C. Nunes, J.J. Bellanger, M. Bedossa, C. Toumoulin, ECG gated tomographic reconstruction for 3-D rotational coronary angiography, in: 2010 Annual International Conference of the IEEE Engineering in Medicine and Biology, IEEE, 2010, pp. 3614–3617, <http://dx.doi.org/10.1109/IEMBS.2010.5627449>.
  - [25] U. Jandt, D. Schäfer, M. Grass, V. Rasche, Automatic generation of 3D coronary artery centerlines using rotational X-ray angiography, *Med. Image Anal.* 13 (6) (2009) 846–858.
  - [26] L. Gu, Y. Zheng, R. Bise, I. Sato, N. Imanishi, S. Aiso, Semi-supervised learning for biomedical image segmentation via forest oriented super pixels (voxels), in: *Medical Image Computing and Computer Assisted Intervention- MICCAI 2017: 20th International Conference*, Quebec City, QC, Canada, September 11–13, 2017, Proceedings, Part I 20, Springer, 2017, pp. 702–710.
  - [27] X. Liu, T. Feng, W. Liu, L. Song, Y. Yuan, W.K. Hau, J. Del Ser, Z. Gao, Scale mutualized perception for vessel border detection in intravascular ultrasound images, *IEEE/ACM Trans. Comput. Biol. Bioinform.* (2022).
  - [28] P. Soille, *Morphological Image Analysis: Principles and Applications*, Springer Science & Business Media, 2013, <http://dx.doi.org/10.1007/978-3-662-05088-0>.
  - [29] G.C. Lehmann, D.W. Holdsworth, M. Drangova, Angle-independent measure of motion for image-based gating in 3D coronary angiography, *Med. Phys.* 33 (5) (2006) 1311–1320.
  - [30] A. Oukili, J.-C. Nunes, Y. Chen, L. Luo, C. Toumoulin, Object-based 3D binary reconstruction from sparse projections in cone beam CT: Comparison of three projection operators, in: 2013 IEEE 10th International Symposium on Biomedical Imaging, IEEE, 2013, pp. 1276–1279, <http://dx.doi.org/10.1109/ISBI.2013.6556764>.
  - [31] N. Otsu, A threshold selection method from gray-level histograms, *IEEE Trans. Syst. Man Cybern.* 9 (1) (1979) 62–66.
  - [32] Y. Cho, D.J. Moseley, J.H. Siewerdsen, D.A. Jaffray, Accurate technique for complete geometric calibration of cone-beam computed tomography systems, *Med. Phys.* 32 (4) (2005) 968–983.
  - [33] M. Xu, C. Zhang, X. Liu, D. Li, Direct determination of cone-beam geometric parameters using the helical phantom, *Phys. Med. Biol.* 59 (19) (2014) 5667.
  - [34] J. Öfverstedt, J. Lindblad, N. Sladoje, Fast and robust symmetric image registration based on distances combining intensity and spatial information, *IEEE Trans. Image Process.* 28 (7) (2019) 3584–3597.
  - [35] S. Klein, M. Staring, J.P.W. Pluim, Evaluation of optimization methods for nonrigid medical image registration using mutual information and B-splines, *IEEE Trans. Image Process.* 16 (12) (2007) 2879–2890.
  - [36] S. Kim, Y. Chang, J.B. Ra, Cardiac image reconstruction via nonlinear motion correction based on partial angle reconstructed images, *IEEE Trans. Med. Imaging* 36 (5) (2017) 1151–1161.
  - [37] C. Rohkohl, G. Lauritsch, A. Keil, J. Hornegger, CAVAREV—an open platform for evaluating 3D and 4D cardiac vasculature reconstruction, *Phys. Med. Biol.* 55 (10) (2010) 2905.
  - [38] C. Schwemmer, C. Rohkohl, G. Lauritsch, K. Müller, J. Hornegger, Residual motion compensation in ECG-gated interventional cardiac vasculature reconstruction, *Phys. Med. Biol.* 58 (11) (2013) 3717.
  - [39] C. Schwemmer, C. Forman, J. Wetzl, A. Maier, J. Hornegger, CoroEval: a multi-platform, multi-modality tool for the evaluation of 3D coronary vessel reconstructions, *Phys. Med. Biol.* 59 (17) (2014) 5163.
  - [40] D. Li, J.C. Carr, S.M. Shea, J. Zheng, V.S. Deshpande, P.A. Wielopolski, J.P. Finn, Coronary arteries: magnetization-prepared contrast-enhanced three-dimensional volume-targeted breath-hold MR angiography, *Radiology* 219 (1) (2001) 270–277.
  - [41] M. Unberath, O. Taubmann, A. Aichert, S. Achenbach, A. Maier, Prior-free respiratory motion estimation in rotational angiography, *IEEE Trans. Med. Imaging* 37 (9) (2018) 1999–2009.